

Article

A Large-Scene Deceptive Jamming Method for Space-Borne SAR Based on Time-Delay and Frequency-Shift with Template Segmentation

Kaizhi Yang ^{1,2}, Wei Ye ¹, Fangfang Ma ^{3,*}, Guojing Li ¹ and Qian Tong ²

¹ Space Engineering University, Beijing 101416, China; yangkaizhi@aliyun.com (K.Y.); yeyuhan@sina.com (W.Y.); leeguojing1014@mail.dlut.edu.cn (G.L.)

² The Unit 94657 of PLA, Jiujiang 332104, China; qianx_tong@sina.cn

³ Logistics Science and Technology Institute, Institute of Systems Engineering, Academy of Military Science, Beijing 100071, China

* Correspondence: fangf_ma@aliyun.com; Tel.: +86-181-9191-8806

Received: 2 December 2019; Accepted: 20 December 2019; Published: 21 December 2019



Abstract: Due to advantages such as its low power consumption and higher concealment, deceptive jamming against synthetic aperture radar (SAR) has received extensive attention during the past decades. However, large-scene deception jamming is still a challenge because of the huge computing burden. In this paper, we propose a new large-scene deceptive jamming algorithm. First, the time-delay and frequency-shift (TDFS) algorithm is introduced to improve the jamming processing speed. The system function of jammer (JSF) for a fake scatterer is simplified to the multiplication of the scattering coefficient, a time-delay term in the range dimension and a frequency-shift term in the azimuth dimension. Then, in order to solve the problem that the effective region of the TDFS algorithm is limited, the scene deceptive jamming template is divided into several blocks according to the SAR parameters and imaging quality control factor. The JSF of each block is calculated by the TDFS algorithm and added together to achieve the large-scene jamming. Finally, the correction algorithm in squint mode is derived. The simplification and parallel-block processing could improve the calculation efficiency significantly. The simulation results verified the validity of the algorithm.

Keywords: synthetic aperture radar (SAR); space-borne SAR; deceptive jamming

1. Introduction

Synthetic aperture radar (SAR) is an effective system that uses electromagnetic waves for high-resolution imaging. Due to the unique advantages of its all-day, all-weather operation, and ability to penetrate camouflage compared with traditional optical remote sensing methods, SAR has become a major means of remote sensing and has been widely used, especially in the military field. At the same time, for the purpose of protecting sensitive targets and regions, electronic countermeasures against SAR have received intensive attention [1–5].

In general, active electronic interference against SAR is divided into two types: barrage jamming and deception jamming. The former uses high-power noise to cover the echo signal from the region of interest (ROI) and makes it impossible to form a clear and distinguishable image [6,7]. The latter emits an echo signal of a false target by the direct generation or modulation–retransmission method, which is mixed with the echo of the real target, affecting the image interpretation process and achieving the purpose of “hidden truth in falsehood” [8–19]. Compared with barrage jamming, deception jamming belongs to a type of smart jamming method which has lower power consumption, higher concealment, and more flexible application scenarios; thus, it is more attractive and does not arouse the awareness of the enemy.

At present, almost all SAR deceptive jamming methods are based on the modulation and retransmission mechanism. In each pulse repetition interval (PRI), according to a series of parameters of the SAR which should be jammed, including kinematic parameters, antenna parameters, and signal parameters, and combining the jamming scene template, the jammer modulates and retransmits the intercepted radar pulse to generate a jamming signal, which will form a false image after range and azimuth compression by the receiver. The deceptive jammer can be regarded as a linear time-invariant (LTI) system in a single PRI. The problem of obtaining the system function of jammer (JSF) is a focus in the field of SAR deceptive jamming. A straightforward method is to calculate the signal propagation delay difference between each scatter in the jamming scene template and the jammer during each PRI [8]. However, this method is computationally intensive and can hardly guarantee real-time processing. Subsequent research has mainly focused on reducing the computational complexity and increasing the processing speed. Usually, parts of the processing are performed in advance to reduce the computational burden during the implementation of jamming. In the specific implementation, this is divided into two categories: azimuth time-domain processing and azimuth frequency-domain processing. The former reduces the computational complexity by approximating the distance equation and is suitable for the broadside or low squint angle mode, including the inverse range-Doppler algorithm [9], phase pre-modulation [10], segmented modulation [11,12], and approach of multiple receivers [13,14]. The latter, including frequency-domain pre-modulation [15], the frequency-domain three-stage algorithm [16], the inverse Omega-K algorithm [17], etc., needs to perform 2-D Fourier transform and Stolt interpolation on the jamming scene template [20,21], which can work under a large squint angle but requires additional information such as the azimuth bandwidth.

Although the methods above improve the computational efficiency of the jamming process to varying degrees, the large computational burden is still the bottleneck of large-scene deceptive jamming for SAR. Zhou etc. proposed a large-scene deceptive jamming method by dividing the jamming scene template into sub-templates according to the depth of focus in the range dimension to simplify the JSF and decomposing the JSF into the slow-time independent terms generated off-line and slow-time dependent terms calculated in real-time [11]. However, this algorithm only works for space-borne SAR operating at the broadside mode, and the computational efficiency is still insufficient. Inspired by this, we propose a new large-scene deceptive jamming algorithm called time-delay and frequency-shift with template segmentation (TDFS-TS). First, the complex modulation process is simplified into the time-delay and frequency-shift operation to increase the computational efficiency. Second, the jamming scene template is divided both in the range dimension and azimuth dimension according to the imaging quality control factor. The correction algorithm in the squint situation is derived as well. Compared with other available deceptive jamming techniques, the proposed method can produce well-focused large deceptive scenes more efficiently.

This paper is organized as follows. Section 2 provides a detailed description of the TDFS-TS algorithm. We begin with the analysis of the basic principles of deceptive jamming against SAR; based on these, we propose the time-delay and frequency-shift (TDFS) jamming algorithm to simplify the process. Then the template segmentation (TS) method is used to achieve large-scene jamming, and the correction algorithm in squint mode is described. In Section 3, the TDFS-TS algorithm is verified by simulation and the computation complexity is analyzed. Section 4 discusses the results and Section 5 concludes this paper.

2. Large-Scene Deceptive Jamming Method Based on TDFS-TS

This section will derive the TDFS-TS deceptive jamming algorithm step by step. First, the principles of deceptive jamming against SAR are introduced. Then the TDFS algorithm is proposed which can significantly improve computational efficiency. The analysis of the jamming signal generated by TDFS shows that the effective region is limited. To solve this problem, the TS method is introduced, and the squint correction algorithm is derived to extend the application scope of the jamming algorithm. Finally, the TDFS-TS algorithm procedure is clarified.

2.1. Principles of Deceptive Jamming against SAR

The principle of SAR deceptive jamming based on modulation–retransmission is presented in Figure 1 [17]. The jammer performs a series of operations including the amplification, down-conversion, analog-to-digital conversion (A/D), and fast Fourier transform (FFT) on the intercepted radar radio frequency (RF) signal to obtain the frequency domain representation of the baseband, while the JSF is calculated based on the template and the SAR parameters including kinematic parameters (platform position, velocity, etc.), antenna parameters (antenna direction, beam pattern, etc.), and signal parameters (carrier frequency, PRI, etc.). Then, we multiply the two and perform an inverse fast Fourier transform (IFFT) to obtain the baseband of the jamming signal and finally perform the digital-to-analog conversion (D/A), up-conversion, gain control, and retransmission. By repeating the above steps for each pulse, a false image can be generated by the receiver. The template is an array of false scatters that depicts the electromagnetic characteristic of the fake scene artificially fabricated by the jammer.

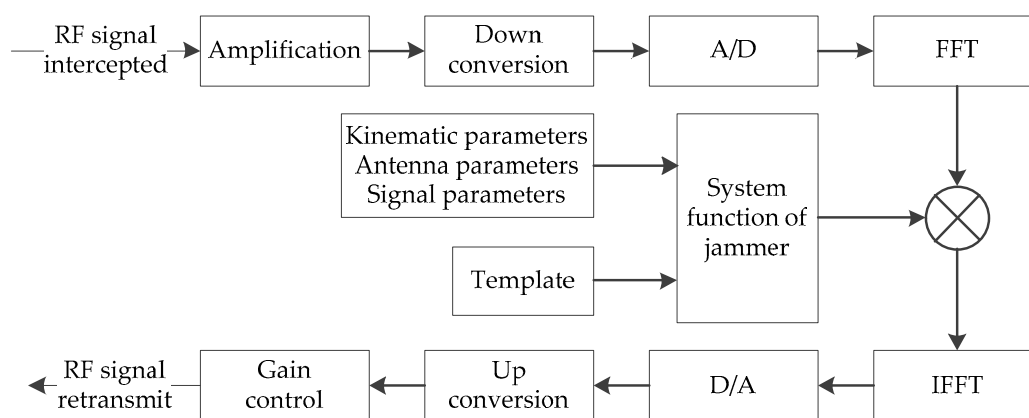


Figure 1. Principle of synthetic aperture radar (SAR) deceptive jamming.

The JSF is the key to the generation of jamming signals. The following illustrates the basic idea for JSF in combination with the geometric model of SAR jamming. As shown in Figure 2, we assume that the SAR platform moves at a constant velocity v and the azimuth time $t_a = 0$ when the plane of zero Doppler passes through the jammer. A Cartesian coordinate system with the location of the jammer as the origin is established in a two-dimensional slant range plane. The x-axis points to the range direction and the y-axis points to the azimuth direction. The shortest slant distance between the jammer and the SAR is R_{J_0} , and the instantaneous slant distance is $R_J(t_a)$ at azimuth time t_a . An arbitrary false point scatterer P is generated by the jammer, the scattering coefficient of P is σ_P and the location is (x, y) in the coordinate above. $R_P(t_a)$ denotes the instantaneous slant distance between P and the jammer.

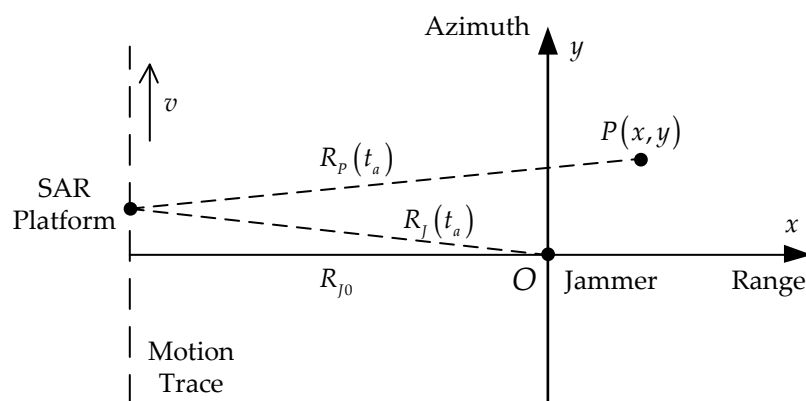


Figure 2. The geometric model of SAR deceptive jamming.

In order to generate the fake point target P in the SAR image, the JSF at azimuth time t_a is [17]

$$H_P(f_r, t_a) = \sigma_P \exp\left[-j2\pi(f_r + f_0) \frac{2\Delta R_P(t_a)}{c}\right], \quad (1)$$

where f_r is the range frequency, c is the velocity of light, $\Delta R_P(t_a)$ is the difference between $R_P(t_a)$ and $R_J(t_a)$:

$$\Delta R_P(t_a) = R_P(t_a) - R_J(t_a) = \sqrt{(x + R_{J0})^2 + (y - vt_a)^2} - \sqrt{R_{J0}^2 + (vt_a)^2}. \quad (2)$$

By calculating the JSF for each scatter in the template T , the JSF for the deception scene can be derived as follows:

$$H(f_r, t_a) = \sum_{P \in T} H_P(f_r, t_a) = \sum_{P \in T} \sigma_P \exp\left[-j2\pi(f_r + f_0) \frac{2\Delta R_P(t_a)}{c}\right]. \quad (3)$$

In the implementation of jamming, the jammer must calculate JSF $H(f_r, t_a)$ and modulate the intercepted signal real-time in each PRI. The calculation of Equation (2) is time-consuming, therefore the method represented by Equation (3) cannot be used directly for large-scene deceptive jamming unless some improvements are made.

2.2. TDFS-TS Algorithm

2.2.1. Deceptive Jamming Based on TDFS

For space-borne SAR, we can assert that $R_{J0} \gg x$, $R_{J0} \gg y$, and $R_{J0} \gg vt_a$ throughout the synthetic aperture time. After the Taylor series expansion, Equation (2) can be approximated as follows [11]:

$$\begin{aligned} \Delta R_P(t_a) &\approx \left[x + R_{J0} + \frac{y^2}{2(x+R_{J0})} - \frac{yvt_a}{x+R_{J0}} + \frac{(vt_a)^2}{2(x+R_{J0})} \right] - \left[R_{J0} + \frac{(vt_a)^2}{2R_{J0}} \right] \\ &\approx x + \frac{y^2}{2R_{J0}} - \frac{yvt_a}{R_{J0}}. \end{aligned} \quad (4)$$

With the approximation above, the JSF—i.e., Equation (1)—can be rewritten as follows:

$$\begin{aligned} H_P(f_r, t_a) &= \sigma_P \exp\left[-j2\pi(f_r + f_0) \left(\frac{2x}{c} + \frac{y^2}{cR_{J0}} - \frac{2yvt_a}{cR_{J0}} \right) \right] \\ &= \sigma_P \exp\left[-j2\pi(f_r + f_0) \frac{2x}{c}\right] \exp\left(j2\pi f_0 \frac{2yvt_a}{cR_{J0}}\right) \\ &\quad \exp\left(-j2\pi f_0 \frac{y^2}{cR_{J0}}\right) \exp\left(j2\pi f_r \frac{2yvt_a - y^2}{cR_{J0}}\right). \end{aligned} \quad (5)$$

where the third exponential term is independent of f_r and t_a and is equivalent to introducing a fixed phase that has no effect on the imaging; thus, it can be ignored. The fourth exponential term can also be omitted when y is small enough (details will be analyzed in the next subsection). Thus, Equation (5) can be simplified as follows:

$$H_P(f_r, t_a) = \sigma_P \exp\left[-j2\pi(f_r + f_0) \frac{2x}{c}\right] \exp\left(j2\pi f_0 \frac{2yvt_a}{cR_{J0}}\right). \quad (6)$$

Actually, at the broadside mode, the azimuth frequency modulation rate of the SAR echo signal from the location of the jammer is [22]

$$K_a = -\frac{2f_0 v^2}{cR_{J0}}. \quad (7)$$

Combined with Equations (6) and (7), we can derive

$$H_P(f_r, t_a) = \sigma_P \exp\left[-j2\pi(f_r + f_0)\frac{2x}{c}\right] \exp\left(-j2\pi K_a \frac{y}{v} t_a\right). \quad (8)$$

This is equivalent to delaying the original echo signal $2x/c$ in fast-time to achieve position deception in the range dimension and a shifting frequency $-K_a y/v$ in slow-time. According to the frequency shifting property of the linear frequency modulation (LFM) signal, the frequency shifting is equivalent to time-delaying y/v in slow-time, which can implement position deception in the azimuth dimension as well.

If the scattering coefficient of the false point target which locates (x, y) in the template is $\sigma(x, y)$, the JSF for the deception scene can be derived as follows:

$$\begin{aligned} H(f_r, t_a) &= \sum_x \sum_y \sigma(x, y) \exp\left[-j2\pi(f_r + f_0)\frac{2x}{c}\right] \exp\left(j2\pi f_0 \frac{2yv t_a}{cR_{J0}}\right) \\ &= \sum_y \exp\left(j4\pi f_0 \frac{yv t_a}{cR_{J0}}\right) \sum_x \sigma(x, y) \exp\left[-j4\pi(f_r + f_0)\frac{x}{c}\right]. \end{aligned} \quad (9)$$

The second summation term in Equation (9) is independent of azimuth time t_a and only related to the relative position of each point in the false scene, which can be calculated off-line to reduce the real-time computational burden. This is the TDFS jamming algorithm, which has the advantages of simplicity and high computational efficiency.

2.2.2. Jamming Signal Analysis

Due to the approximation and simplification, the TDFS algorithm has high computational efficiency. However, the approximation and simplification will cause a decline in the image quality of the deceptive target at the same time. In this subsection, we will analyze the impact of the simplified operations above on the imaging results by comparing the difference between the jamming signal and real point target echo in the range-Doppler domain [23].

The echo signal of a real scatter point $P(x, y)$ is represented as follows [22]:

$$s_P(t_r, t_a) = \sigma_P w_a(t_a) w_r\left[t_r - \frac{2R_P(t_a)}{c}\right] \exp\left[-j4\pi f_0 \frac{R_P(t_a)}{c}\right] \exp\left\{j\pi K_r \left[t_r - \frac{2R_P(t_a)}{c}\right]^2\right\}, \quad (10)$$

where $w_a(t_a)$ represents the azimuth amplitude, $w_r(t_r)$ is the SAR pulse complex envelope, and K_r is the frequency modulation rate of the SAR pulse.

The parabolic approximation of the instantaneous slant range $R_P(t_a)$ by Taylor series is [22]

$$R_P(t_a) = \sqrt{(x + R_{J0})^2 + (y - vt_a)^2} = x + R_{J0} + \frac{(y - vt_a)^2}{2(x + R_{J0})}. \quad (11)$$

We can derive the echo signal expression (12) of the real target point $P(x, y)$ in the range-Doppler domain by bringing Equation (11) into Equation (10) and using the principle of stationary phase (POSP) [22]:

$$\begin{aligned} S_P(t_r, f_a) &= \sigma_P W_a(f_a) w_r\left[t_r - \frac{2R_P(f_a)}{c}\right] \\ &\exp\left\{j\pi K_r \left[t_r - \frac{2R_P(f_a)}{c}\right]^2 - j\pi \frac{f_a^2}{K_a} - j2\pi f_a \frac{y}{v} - j4\pi f_0 \frac{x + R_{J0}}{c}\right\}, \end{aligned} \quad (12)$$

where $R_P(f_a)$ is the range cell migration (RCM) curve of the target in the range-Doppler domain:

$$R_P(f_a) = x + R_{J0} + \frac{(x + R_{J0})c^2}{8v^2 f_a^2}, \quad (13)$$

and the azimuth frequency modulation rate is

$$K_a = -\frac{2v^2 f_0}{c(x + R_{J0})}. \quad (14)$$

The echo signal will focus on the coordinate (x, y) after range compression, RCM correction (RCMC), and azimuth compression.

For comparison, when the JSF is Equation (8), the jamming signal is expressed as follows:

$$s_J(t_r, t_a) = \sigma_P w_a(t_a) w_r \left[t_r - \frac{2R_J(t_a)}{c} - \frac{2x}{c} \right] \exp \left\{ -j4\pi f_0 \left[\frac{R_J(t_a)}{c} + \frac{x}{c} - \frac{yvt_a}{cR_{J0}} \right] \right\} \exp \left\{ j\pi K_r \left[t_r - \frac{2R_J(t_a)}{c} - \frac{2x}{c} \right]^2 \right\}. \quad (15)$$

Similarly, the parabolic approximation and POSP is used to obtain the expression of the jamming signal in the range-Doppler domain:

$$S_J(t_r, f_a) = \sigma_P W_a(f_a) w_r \left[t_r - \frac{2R_{JP}(f_a)}{c} \right] \exp \left\{ j\pi K_r \left[t_r - \frac{2R_{JP}(f_a)}{c} \right]^2 - j\pi \frac{f_a^2}{K_{fa}} - j2\pi f_a \frac{y}{v} - j4\pi f_0 \frac{x + R_{J0}}{c} + j2\pi f_0 \frac{y^2}{cR_{J0}} \right\}, \quad (16)$$

where the RCM of fake target is

$$R_{JP}(f_a) = x + R_{J0} + \frac{R_{J0}c^2}{8v^2 f_0^2} f_a^2 - \frac{yc}{2vf_0} f_a + \frac{y^2}{2R_{J0}}, \quad (17)$$

and the azimuth frequency modulate rate of jamming signal is

$$K_{Ja} = -\frac{2v^2 f_0}{cR_{J0}}. \quad (18)$$

It can be found that there are differences between the real target echo signal and the jamming signal in the RCM curve and azimuth frequency modulation rate, ignoring the phase terms unrelated to pulse compression. The effects of these differences on the imaging results and the corresponding effective region of deceptive jamming are analyzed in detail below.

First, it is obvious that the jamming signal introduces the azimuth frequency modulation rate error, which will cause a mismatch of the azimuth matched filter and finally lead to the main lobe broadening of the azimuth pulse compression result. The azimuth frequency modulation rate error is

$$\Delta K_a = K_{Ja} - K_a = -\frac{2v^2 f_0 x}{cR_{J0}(x + R_{J0})}. \quad (19)$$

The effect of ΔK_a on the main lobe broadening can be measured by the quadratic phase error (QPE); the expression of QPE is as follows [22]:

$$\text{QPE} = \pi \Delta K_a \left(\frac{T}{2} \right)^2 = -\frac{2\pi v^2 f_0 x}{cR_{J0}(x + R_{J0})} \left(\frac{L}{2v} \right)^2, \quad (20)$$

where $T = L/v$ is the synthetic aperture time and L represents the synthetic aperture length.

For a typical Kaiser window with $\beta = 2.5$, if the broadening is required to be less than 2%, 5%, and 10%, the corresponding QPE absolute value should be less than 0.27π , 0.41π , and 0.55π [22]. Here,

we define the azimuth QPE factor ε ; when the condition $|\text{QPE}| \leq \varepsilon\pi$ is required, the range coordinate x should satisfy

$$|x| \leq \frac{2\varepsilon c R_{J0}(x + R_{J0})}{f_0 L^2} \approx 2\varepsilon \frac{c}{f_0} \left(\frac{R_{J0}}{L} \right)^2. \quad (21)$$

Second, in the range-Doppler domain, the RCM error of the jamming signal is

$$\Delta R_P(f_a) = R_{JP}(f_a) - R_P(f_a) = -\frac{xc^2}{8v^2 f_0^2} f_a^2 - \frac{yc}{2vf_0} f_a + \frac{y^2}{2R_{J0}}. \quad (22)$$

The last term in Equation (22) can be omitted because $R_{J0} \gg y$. The residual RCM introduced by $\Delta R_P(f_a)$ in broadside mode is represented as follows:

$$\text{RCM}_{\text{res}} = \left| \Delta R_P\left(\frac{B_a}{2}\right) - \Delta R_P\left(-\frac{B_a}{2}\right) \right| = \frac{B_a c}{2vf_0} |y|, \quad (23)$$

where B_a is the azimuth Doppler bandwidth and can be expressed as [22]

$$B_a = \frac{L}{v} |K_{Ja}| = \frac{2vf_0 L}{cR_{J0}}. \quad (24)$$

Combined with Equations (23) and (24), we can simplify the expression of residual RCM:

$$\text{RCM}_{\text{res}} = \frac{L}{R_{J0}} |y|. \quad (25)$$

The residual RCM will result in the main lobe broadening in both range and azimuth dimensions and the extent of broadening can be measured by the ratio of the residual RCM to the range resolution. The range resolution $\rho_r \approx c/2B$, where B is the signal bandwidth. Then, we define the residual RCM factor η ; if we require $\text{RCM}_{\text{res}} \leq \eta\rho_r$, the azimuth coordinate y should satisfy

$$|y| \leq \eta \frac{\rho_r R_{J0}}{L} = \eta \frac{cR_{J0}}{2BL}. \quad (26)$$

According to [22], the residual RCM should be no more than 0.5 of the range cell; therefore, η should be no more than 0.5.

In addition, due to the difference between the false and real point targets in the instantaneous slant range history, the Doppler center frequency of the jamming signal shifts, and the azimuth main lobe broadening and ghost targets are introduced. This phenomenon limits the effective azimuth scale as well; according to [11], the azimuth coordinate y should satisfy

$$|y| \leq \frac{cR_{J0}}{2vf_0} \left(\text{PRF} - \frac{v}{D} \right) - \frac{L}{2}, \quad (27)$$

where PRF is the pulse repetition frequency and D is the antenna aperture in the azimuth direction.

Equations (21) and (26) describe the effective region of the range and azimuth directions of the TDFS algorithm with the specified azimuth QPE factor ε and residual RCM factor η . The jamming signals representing the false target located beyond the region will not achieve the desired deception. Equation (27) described the inherent limitations of SAR deceptive jamming in the azimuth direction, which is beyond the scope of this article. In the following discussion, we suppose that the size of the template in the azimuth dimension meets the requirement of Equation (27). When the typical C-band space-borne SAR parameters (see Table 1 in Section 3) are set as an example, we can calculate the effective region: $|x| \leq 1.25$ km and $|y| \leq 0.75$ km with $\varepsilon = 0.25$ and $\eta = 0.5$; i.e., a rectangular area of 2.5 km \times 1.5 km.

Table 1. The setting of SAR parameters in simulations.

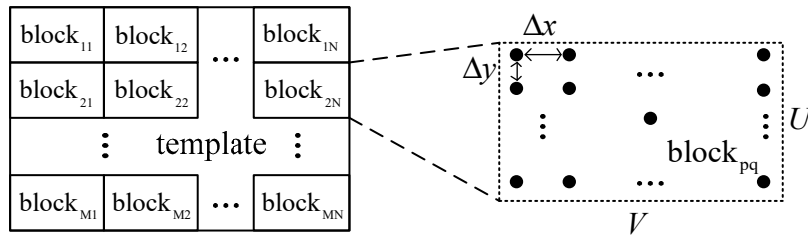
Carrier Frequency	Chirp Rate	PRI	Pulse Width	Platform Velocity	Shortest Slant Range	Antenna Aperture
5.30 GHz	0.72 MHz/ μ s	0.79 ms	41.74 μ s	7.06 km/s	989 km	10 m

2.2.3. Template Segmentation

The analysis in the previous subsection shows that the effective region of the TDFS algorithm is limited. In order to achieve deceptive jamming in a larger scene, we divide the jamming scene template into several blocks and apply a time-delay and frequency-shift in each block to calculate the partial JSF, which will be summed to get the JSF on the whole template. As shown in Figure 3, the template consisting of $m \times n$ point scatters is divided into $M \times N$ blocks; each block contains $U \times V$ point scatters, namely $U = m/M$ and $V = n/N$. If the range interval between each point is Δx and the azimuth interval is Δy , U and V should satisfy the following conditions according to the limitation of the effective region Equations (21) and (26) with the required ε and η :

$$U \leq \eta \frac{cR_{min}}{BL\Delta y}, \quad V \leq 4\varepsilon \frac{c}{f_0\Delta x} \left(\frac{R_{min}}{L} \right)^2, \quad (28)$$

where R_{min} is the minimum value of the shortest slant range of all point scatters, which can be approximated by R_{J0} .

**Figure 3.** Jamming scene template segmentation diagram.

The scattering coefficients of point scatters in block_{pq} can be expressed as a matrix \mathbf{T}_{pq} :

$$\mathbf{T}_{pq} = \begin{bmatrix} \sigma_{11} & \sigma_{12} & \cdots & \sigma_{1V} \\ \sigma_{21} & \sigma_{22} & \cdots & \sigma_{2V} \\ \vdots & \vdots & \ddots & \vdots \\ \sigma_{U1} & \sigma_{U2} & \cdots & \sigma_{UV} \end{bmatrix}. \quad (29)$$

Suppose the coordinate of the block_{pq} geometric center is (x_q, y_p) , where $p = 1, 2, \dots, M$ and $q = 1, 2, \dots, N$. According to Equations (1) and (2), the JSF on the block_{pq} geometry center $H_{c_{pq}}(f_r, t_a)$ is represented as follows:

$$H_{c_{pq}}(f_r, t_a) = \exp \left\{ -\frac{j4\pi(f_r + f_0)}{c} \left[\sqrt{(x_q + R_{J0})^2 + (y_p - vt_a)^2} - \sqrt{R_{J0}^2 + (vt_a)^2} \right] \right\}. \quad (30)$$

The jamming signal generated by $H_{c_{pq}}(f_r, t_a)$ can generate a well-focused point target in the center of block_{pq} after imaging, which is equivalent to moving the jammer to the geometric center of block_{pq} .

Then, we use the TDFS algorithm to generate the JSF on block_{pq}:

$$H_{pq}(f_r, t_a) = Hc_{pq}(f_r, t_a) \sum_{k=1}^U \exp\left[\frac{j4\pi f_0 v t_a \Delta y}{c(R_{J0} + x_q)} \left(k - \frac{U+1}{2}\right)\right] \sum_{l=1}^V \sigma_{kl} \exp\left[-\frac{j4\pi(f_0 + f_r) \Delta x}{c} \left(l - \frac{V+1}{2}\right)\right], \quad (31)$$

where σ_{kl} is the element of row k and column l in the matrix \mathbf{T}_{pq} . Finally, the JSF on the whole template can be derived by summing JSF on all blocks:

$$H(f_r, t_a) = \sum_{p=1}^M \sum_{q=1}^N H_{pq}(f_r, t_a). \quad (32)$$

Since the number of blocks is very small compared to the total number of scatters in the template, Equation (30) has a limited effect on the computing load. In addition, the second summation term of Equation (31) is independent of slow time t_a and can be calculated offline. The template segmentation method can solve the problem that the effective region of the TDFS algorithm is limited and achieve the purpose of the rapid generation of large scene deceptive jamming signals.

2.2.4. Correction Algorithm in Squint Mode

The analyses above are based on the broadside mode with the squint angle $\theta = 0$. In order to extend the broadside jamming algorithm to squint mode, this subsection will discuss the effect of the squint angle on the jamming result and the corresponding correction method. It should be pointed out that the parabolic approximation of the instantaneous slant range in Equation (4) will no longer be applicable under the condition of a large squint angle, so the jamming method of this article is limited to the small squint angle and the medium aperture length SAR.

First, the Doppler center frequency of the echo signal $f_{ac} = 2vf_0 \sin \theta / c$, the presence of the squint angle will result in the non-zero Doppler center frequency. At this time, the azimuth signal can be regarded as the non-baseband signal, and the frequency modulation rate error will cause the position offset besides main lobe broadening in pulse compression [22]. According to the pulse compression principle [22], the azimuth main lobe position offset of scatter with coordinate (x, y) is

$$y_{ofs}(x, y) = -\frac{\Delta K_a}{K_a} t_{ac} v = x \tan \theta, \quad (33)$$

where $t_{ac} = -R_{J0} \tan \theta / v$ is the pulse center time of the jamming signal in the azimuth dimension.

On the other hand, when $f_{ac} \neq 0$, the RCM error will cause the RCM curve to shift along the range dimension in addition to introducing the residual RCM, causing main lobe broadening. According to Equation (22), the offset in the range dimension of fake point $P(x, y)$ is

$$x_{ofs}(x, y) = \Delta R_P(f_{ac}) \approx -\frac{x}{2} \sin^2 \theta - y \sin \theta. \quad (34)$$

The residual RCM will increase at the same time:

$$\text{RCM}_{\text{res}} = \left| \Delta R_P\left(f_{ac} + \frac{B_a}{2}\right) - \Delta R_P\left(f_{ac} - \frac{B_a}{2}\right) \right| = \left| \frac{B_a c}{2v f_0} y + \frac{B_a c \sin \theta}{4v f_0} x \right|. \quad (35)$$

In order to ensure the image quality of the fake scene, the size of the blocks should be reduced. However, the RCM_{res} increment is not obvious when the squint angle is small. Thus, it can be ignored in this paper.

According to the analysis above, the main effect of the squint angle is the location offset of fake targets in the deceptive image, and the offset depends on the coordinates in the template. This effect

will cause the distortion of the jamming image. Therefore, the coordinates of each scatter in the template should be corrected. For the false scatter with coordinate (x, y) , the corrected coordinate (x_c, y_c) can be represented as follows:

$$\begin{cases} x_c = x - x_{ofs}(x, y) = x + \frac{x}{2} \sin^2 \theta + y \sin \theta, \\ y_c = y - y_{ofs}(x, y) = y - x \tan \theta. \end{cases} \quad (36)$$

Correspondingly, Equation (31) will be modified as follows:

$$\begin{aligned} H_{pq}(f_r, t_a) = H_{Cpq}(f_r, t_a) \sum_{k=1}^U \sum_{l=1}^V \sigma_{kl} \exp \left\{ -\frac{j4\pi(f_r+f_0)\Delta x}{c} \left[\left(1 + \frac{\sin^2 \theta}{2}\right) \left(l - \frac{V+1}{2}\right) \right. \right. \\ \left. \left. + \Delta y \sin \theta \left(k - \frac{U+1}{2}\right) \right] \right\} \exp \left\{ \frac{j4\pi f_0 v t_a}{c(R_{j0}+x_q)} \left[-\Delta x \tan \theta \left(l - \frac{V+1}{2}\right) + \Delta y \left(k - \frac{U+1}{2}\right) \right] \right\}. \end{aligned} \quad (37)$$

The range and azimuth-related terms in Equation (37) are separable, so Equation (37) can be rewritten as matrix operations to increase the calculation speed. Here, we define the time-delay matrixes \mathbf{Hr}_1 , \mathbf{Hr}_2 and frequency-shift matrixes \mathbf{Ha}_{q1} , \mathbf{Ha}_{q2} :

$$\mathbf{Hr}_1 = \begin{bmatrix} \exp \left[-\frac{j4\pi(f_r+f_0)\Delta x}{c} \left(1 + \frac{\sin^2 \theta}{2}\right) \left(1 - \frac{V+1}{2}\right) \right] \\ \exp \left[-\frac{j4\pi(f_r+f_0)\Delta x}{c} \left(1 + \frac{\sin^2 \theta}{2}\right) \left(2 - \frac{V+1}{2}\right) \right] \\ \vdots \\ \exp \left[-\frac{j4\pi(f_r+f_0)\Delta x}{c} \left(1 + \frac{\sin^2 \theta}{2}\right) \left(V - \frac{V+1}{2}\right) \right] \end{bmatrix}, \quad (38)$$

$$\mathbf{Hr}_2 = \begin{bmatrix} \exp \left[-\frac{j4\pi(f_r+f_0)\Delta y \sin \theta}{c} \left(1 - \frac{U+1}{2}\right) \right] \\ \exp \left[-\frac{j4\pi(f_r+f_0)\Delta y \sin \theta}{c} \left(2 - \frac{U+1}{2}\right) \right] \\ \vdots \\ \exp \left[-\frac{j4\pi(f_r+f_0)\Delta y \sin \theta}{c} \left(U - \frac{U+1}{2}\right) \right] \end{bmatrix}, \quad (39)$$

$$\mathbf{Ha}_{q1} = \begin{bmatrix} \exp \left[-\frac{j4\pi f_0 v t_a \Delta x \tan \theta}{c(R_{j0}+x_q)} \left(1 - \frac{V+1}{2}\right) \right] \\ \exp \left[-\frac{j4\pi f_0 v t_a \Delta x \tan \theta}{c(R_{j0}+x_q)} \left(2 - \frac{V+1}{2}\right) \right] \\ \vdots \\ \exp \left[-\frac{j4\pi f_0 v t_a \Delta x \tan \theta}{c(R_{j0}+x_q)} \left(V - \frac{V+1}{2}\right) \right] \end{bmatrix}, \quad (40)$$

$$\mathbf{Ha}_{q2} = \begin{bmatrix} \exp \left[\frac{j4\pi f_0 v t_a \Delta y}{c(R_{j0}+x_q)} \left(1 - \frac{U+1}{2}\right) \right] \\ \exp \left[\frac{j4\pi f_0 v t_a \Delta y}{c(R_{j0}+x_q)} \left(2 - \frac{U+1}{2}\right) \right] \\ \vdots \\ \exp \left[\frac{j4\pi f_0 v t_a \Delta y}{c(R_{j0}+x_q)} \left(U - \frac{U+1}{2}\right) \right] \end{bmatrix}. \quad (41)$$

Equation (37) is rewritten as follows:

$$H_{pq}(f_r, t_a) = H_{Cpq}(f_r, t_a) \left[\left(\mathbf{Hr}_2 \circ \mathbf{Ha}_{q2} \right)^T \mathbf{T}_{pq} \left(\mathbf{Hr}_1 \circ \mathbf{Ha}_{q1} \right) \right], \quad (42)$$

where $(\cdot)^T$ represents the matrix transposition and the operator \circ represents the Hadamard product of the matrix.

We can get the JSF on the entire scene by superimposing the JSF on all blocks, which is the same as Equation (32). The time-delay matrixes \mathbf{Hr}_1 and \mathbf{Hr}_2 are independent of the azimuth time t_a , which can be calculated offline in advance to improve the real-time processing speed.

2.3. TDFS-TS Algorithm Procedure

The prerequisite for the successful implementation of SAR deceptive jamming is to obtain relevant intelligence on the jamming object, which mainly includes the follows aspects.

- Kinematic parameters of the SAR platform, including motion trajectory, motion velocity v , etc. The motion trajectory information is used to establish the jamming coordinate system and determine R_{j0} , the shortest distance between the jammer and SAR;
- Antenna parameters, including the squint angle θ , synthetic aperture length L , etc.;
- Signal parameters, including the carrier frequency f_0 , bandwidth B , PRI, etc.

The specific detection methods of the parameters above will not be discussed in this paper; we simply suppose that the parameters have been obtained in advance.

As shown in Figure 4, the entire procedure includes two parts: preprocessing and real-time calculation. The first step in the preprocessing stage is template segmentation: according to the parameters including synthetic aperture length L , signal bandwidth B , shortest slant range of the jammer R_{j0} and the given factors ε and η , we divide the template into several blocks based on the limitation of Equation (28); then, we perform offline calculation and calculate the time-delay matrixes \mathbf{Hr}_1 and \mathbf{Hr}_2 according to Equations (38) and (39). In the real-time calculation stage, we calculate frequency-shift matrixes \mathbf{Ha}_{q1} , \mathbf{Ha}_{q2} according to Equations (40) and (41); then, we calculate the JSF on each block based on Equations (30) and (42); finally, we add the JSF on all blocks to obtain the JSF on the entire scene.

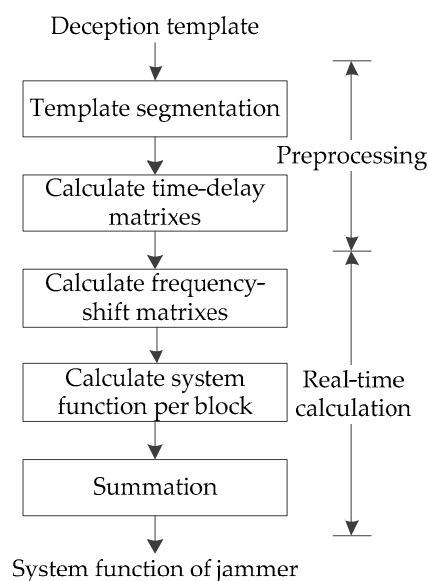


Figure 4. Time-delay and frequency-shift with template segmentation (TDFS-TS) algorithm procedure.

3. Simulation Results

In this section, the effectiveness of the TDFS-TS algorithm is verified by simulating the imaging results of false point targets and fake scenes, and the computational complexity is analyzed. The simulation results of the range dimension segmentation (RDS) algorithm proposed by Zhou et al. [11] are used as a comparison. The main parameters of the radar, which reference the satellite RADARSAT-1, are listed in Table 1.

3.1. Fake Point Scatters Case

In order to analyze the imaging result of fake point scatter at different positions after imaging, a deceptive scene template containing only four-point scatters is set as shown in Figure 5. The four points $P_0 \sim P_3$ are arranged in a rectangular shape with a distance of 6 km in the range dimension and 2 km in the azimuth dimension. According to the calculation results in Section 2.2.2, we set the length of blocks to 2.5 km in the range dimension and 1.5 km in the azimuth dimension. Since the imaging quality of fake scatters is only related to the position in the block, for the purpose of analyzing the jamming effect of the algorithm comprehensively, the template segmentation scheme is shown by the dashed line in Figure 5, meaning that P_0 is located at the center of block 1, P_1 is at the edge of block 3 in the range dimension, P_2 is at the azimuth edge of block 4, and P_3 is at the edge of block 6 in both range and azimuth dimensions. In addition, the position of the jammer (i.e., the origin position) is set at the point P_0 ; actually, the position of the jammer has little effect on the imaging result. In the simulation of the RDS algorithm, the template is divided into three segments with the same segmentation length (2.5 km) in the range dimension and is no longer segmented in the azimuth dimension.

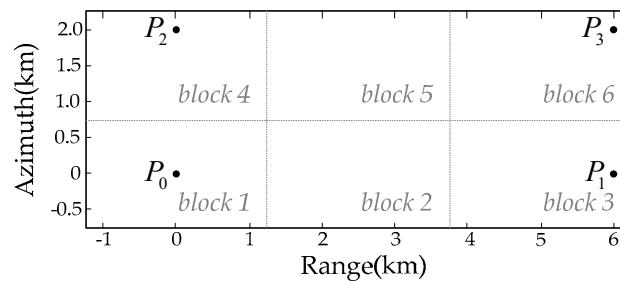


Figure 5. The deceptive scene containing four-point scatters.

Figures 6–9 show the imaging results of the four scatters by the RDS and TDFS-TS algorithm in the broadside mode and squint mode with the squint angle $\theta = 5^\circ$, including the close-up image, range profile, and azimuth profile. Tables 2 and 3 list the imaging quality parameters of range and azimuth dimensions in the two modes, including 3 dB impulse response width (IRW), main lobe position offset (MLPO), peak sidelobe ratio (PSLR), and integrated sidelobe ratio (ISLR). It can be seen that, compared with the RDS algorithm, the performance of the TDFS-TS algorithm is basically equivalent, the RDS algorithm is more advantageous on IRW, while TDFS-TS is dominant over MLPO. The IRW of TDFS-TS algorithm is increased especially for the azimuth dimension in squint mode; however, the maximum broadening does not exceed 3.6%. In the squint mode, the MLPO of the RDS algorithm can reach up to -80.32 m in the azimuth dimension, which can be eliminated basically by the TDFS-TS algorithm due to the corresponding correction. Because of the influence of the residual RCM, the MLPO in the range dimension cannot be completely corrected, but the overall image is affected very little. In short, the simulation of fake point scatters shows that the TDFS-TS algorithm is effective and has certain advantages in several areas.

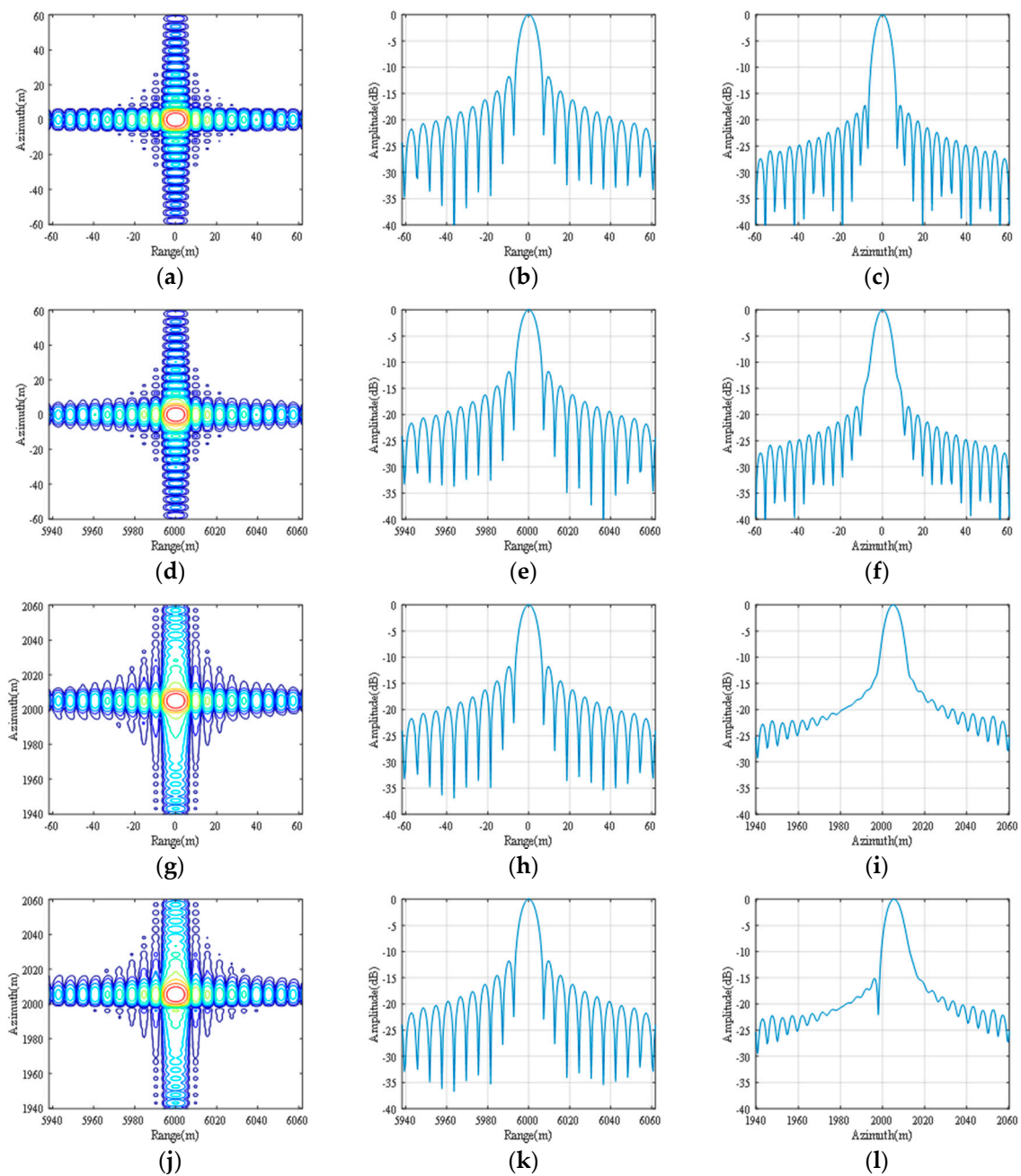


Figure 6. Simulation results of the RDS algorithm for false point scatters in broadside mode. (a–c) are the close-up image, range profile, and azimuth profile of P_0 , respectively; (d–f) are the close-up image, range profile, and azimuth profile of P_1 respectively; (g–i) are the close-up image, range profile, and azimuth profile of P_2 , respectively; (j–l) are the close-up image, range profile, and azimuth profile of P_3 , respectively.

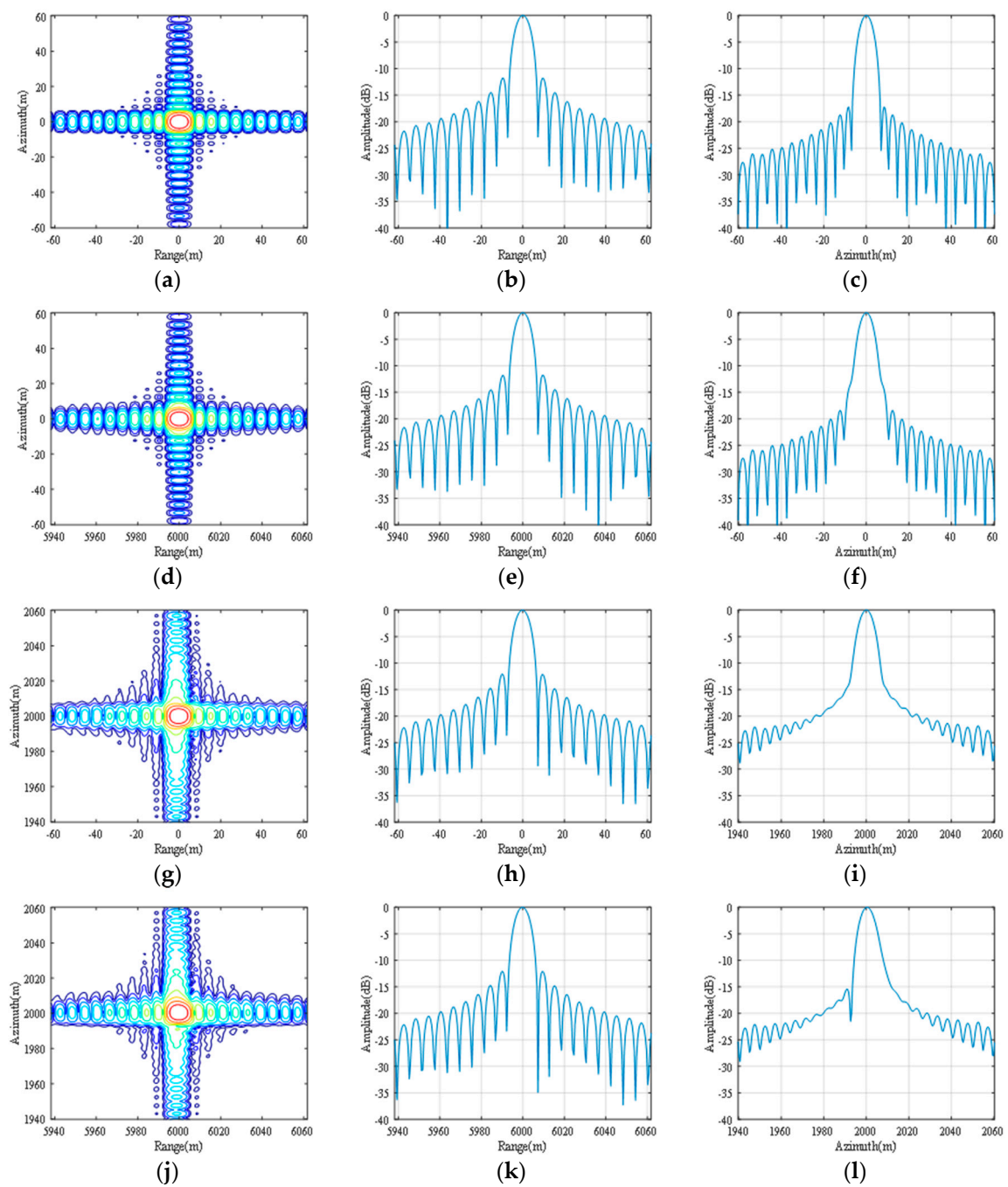


Figure 7. Simulation results of the TDFS-TS algorithm for false point scatters in broadside mode. (a–c) are the close-up image, range profile, and azimuth profile of P_0 , respectively; (d–f) are the close-up image, range profile, and azimuth profile of P_1 , respectively; (g–i) are the close-up image, range profile, and azimuth profile of P_2 , respectively; (j–l) are the close-up image, range profile, and azimuth profile of P_3 , respectively.

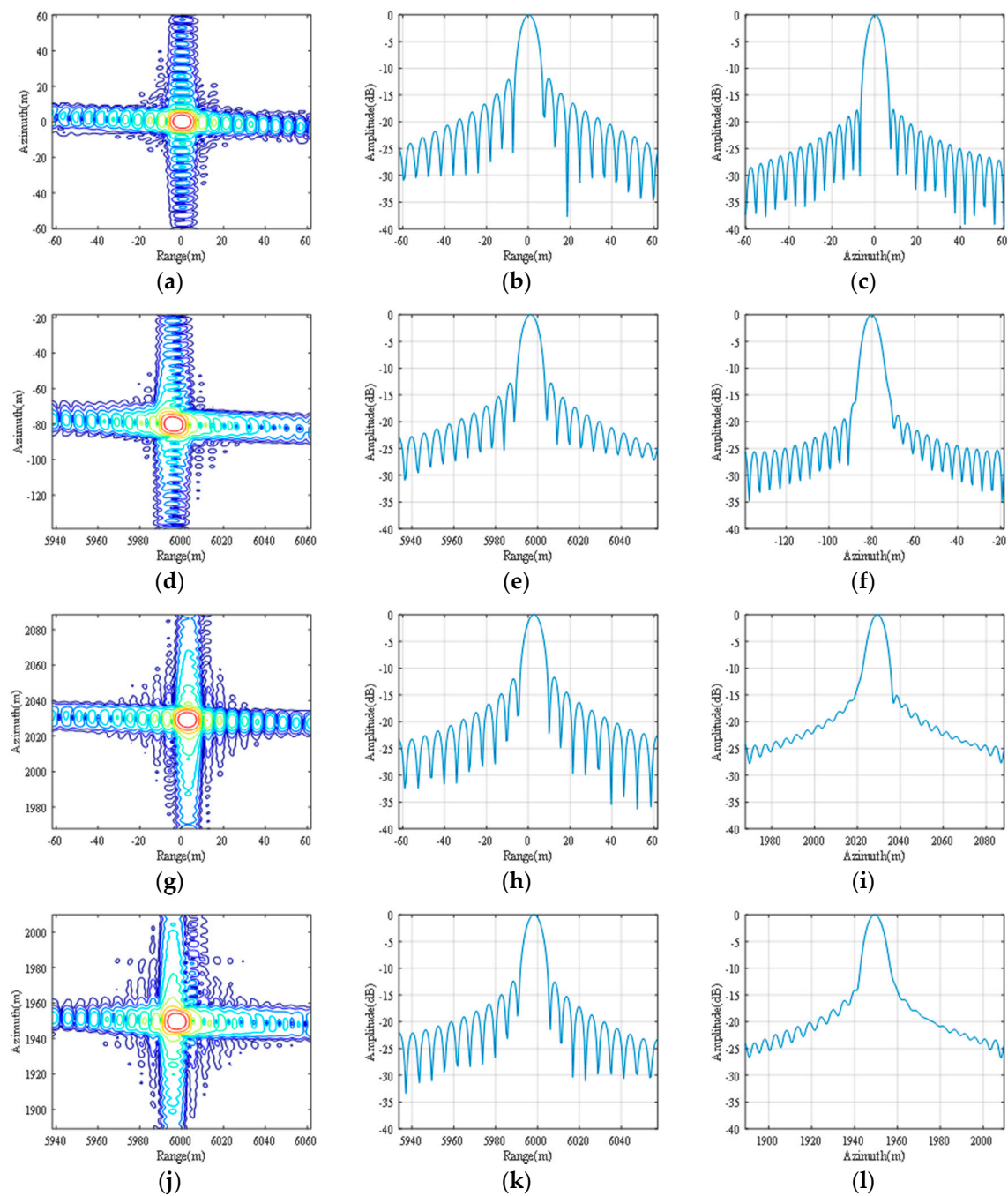


Figure 8. Simulation results of the RDS algorithm for false point scatters in squint mode with a squint angle $\theta = 5^\circ$. (a–c) are the close-up image, range profile, and azimuth profile of P_0 , respectively; (d–f) are the close-up image, range profile, and azimuth profile of P_1 , respectively; (g–i) are the close-up image, range profile, and azimuth profile of P_2 , respectively; (j–l) are the close-up image, range profile, and azimuth profile of P_3 , respectively.

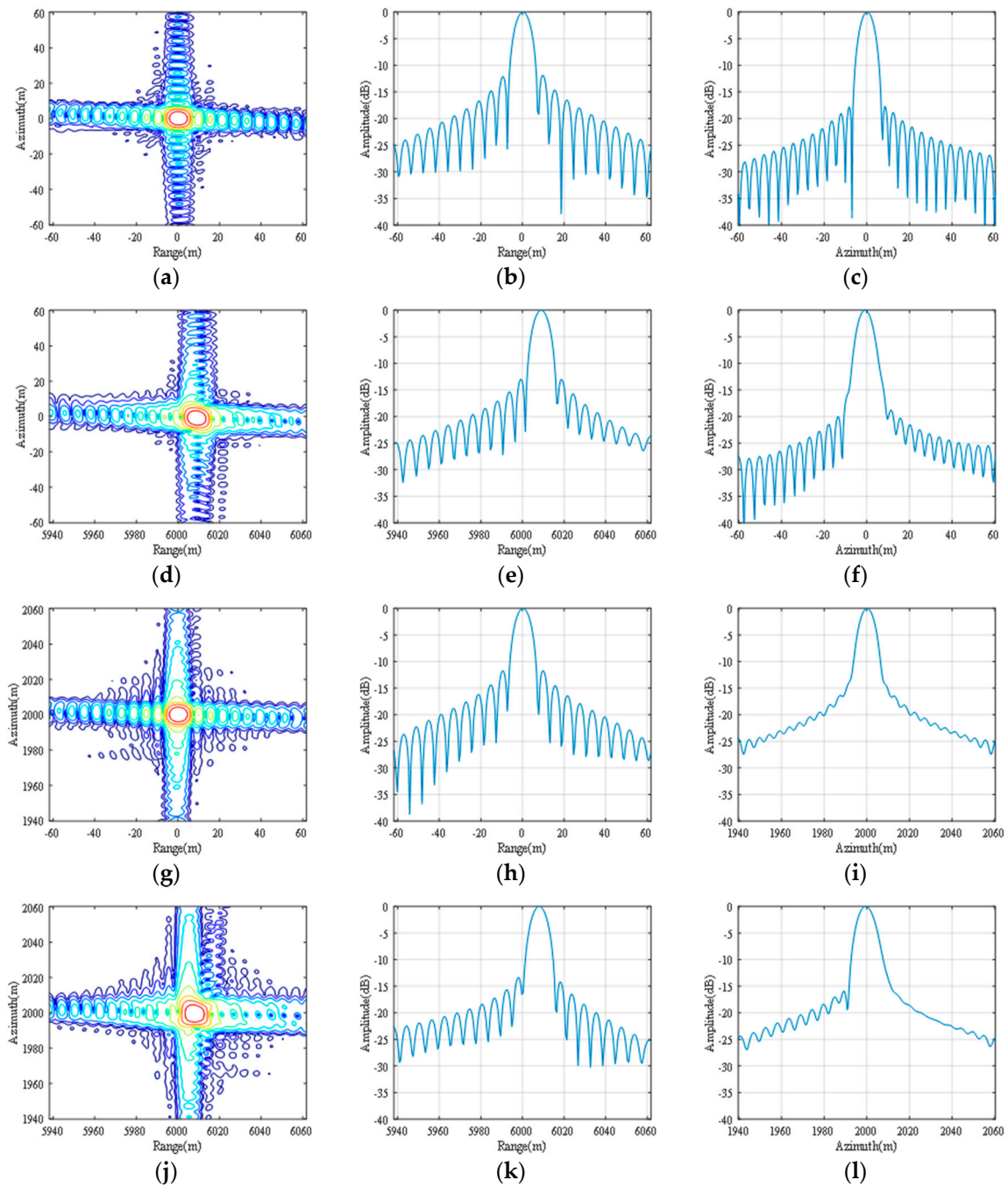


Figure 9. Simulation results of the TDFS-TS algorithm for false point scatters in squint mode with a squint angle $\theta = 5^\circ$. (a–c) are the close-up image, range profile, and azimuth profile of P_0 , respectively; (d–f) are the close-up image, range profile, and azimuth profile of P_1 , respectively; (g–i) are the close-up image, range profile, and azimuth profile of P_2 , respectively; (j–l) are the close-up image, range profile, and azimuth profile of P_3 , respectively.

Table 2. Comparison of imaging quality parameters between the RDS algorithm and TDFS-TS algorithm in broadside mode.

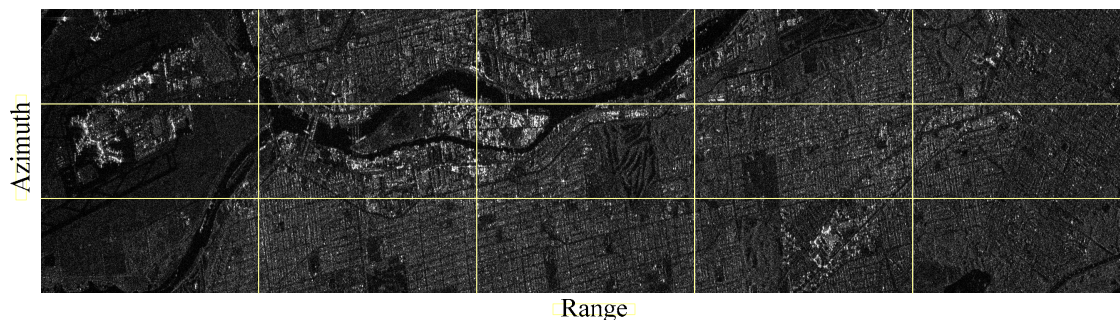
		Range Dimension				Azimuth Dimension			
		IRW (m)	MLPO (m)	PSLR (dB)	ISLR (dB)	IRW (m)	MLPO (m)	PSLR (dB)	ISLR (dB)
P_0	RDS	7.73	0	-11.78	-12.57	6.77	0	-17.24	-19.50
	TDFS-TS	7.73	0	-11.78	-12.57	6.77	0	-17.24	-19.50
P_1	RDS	7.73	0	-11.78	-12.57	6.88	0	-13.47	-15.05
	TDFS-TS	7.73	0	-11.78	-12.57	6.88	0	-13.39	-14.98
P_2	RDS	7.73	0	-11.78	-12.57	7.39	5.04	-14.46	-14.90
	TDFS-TS	7.78	-0.21	-12.03	-12.96	7.47	0	-13.95	-13.67
P_3	RDS	7.73	0	-11.77	-12.57	7.53	5.52	-15.03	-14.24
	TDFS-TS	7.78	-0.21	-12.04	-12.96	7.60	0.48	-15.12	-12.55

Table 3. Comparison of imaging quality parameters between the range dimension segmentation (RDS) algorithm and TDFS-TS algorithm in squint mode with squint angle $\theta = 5^\circ$.

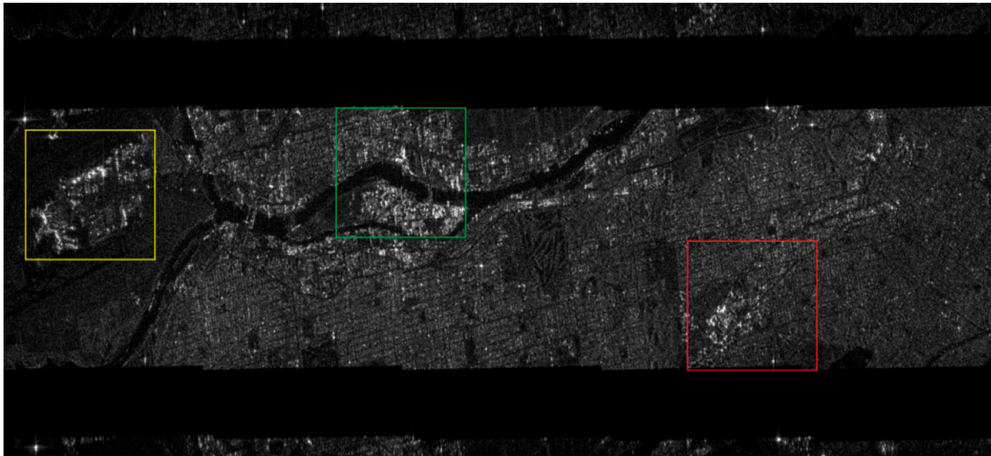
		Range Dimension				Azimuth Dimension			
		IRW (m)	MLPO (m)	PSLR (dB)	ISLR (dB)	IRW (m)	MLPO (m)	PSLR (dB)	ISLR (dB)
P_0	RDS	7.73	0	-12.07	-12.79	6.77	0	-17.79	-20.30
	TDFS-TS	7.73	0	-12.07	-12.79	6.77	0	-17.79	-20.30
P_1	RDS	7.88	-3.48	-12.79	-13.87	7.07	-80.32	-16.56	-17.91
	TDFS-TS	7.88	7.69	-12.94	-13.92	7.15	-0.98	-18.76	-17.83
P_2	RDS	7.77	2.46	-12.02	-12.60	7.39	29.01	-15.03	-15.45
	TDFS-TS	7.74	0.01	-11.68	-12.48	7.34	-0.01	-14.59	-14.96
P_3	RDS	7.95	-1.17	-12.36	-13.47	8.05	-50.70	-14.05	-14.08
	TDFS-TS	8.16	7.73	-13.29	-14.87	8.34	-0.57	-15.95	-14.28

3.2. General Deceptive Scene Case

In this subsection, the TDFS-TS algorithm is applied to yield a fake scene. The jamming object is RADARSAT-1, whose parameters are listed in Table 1, and the squint angle $\theta \approx -1.58^\circ$. The raw data of the radar are obtained from the appendix in [22]. The fake scene template is another SAR image, as shown in Figure 10, whose length in the range dimension is 12.5 km and 4.5 km in the azimuth dimension. We divide the template according to the same block size calculated in Section 2.2.2, as shown by the yellow line in Figure 10.

**Figure 10.** Deceptive jamming template with 12.5 km in the range dimension and 4.5 km in the azimuth dimension, which is divided into blocks by the yellow line. The block size is 2.5 km \times 1.5 km.

First, the signals generated by the two algorithms are processed to get the images which are shown in Figure 11 after being amplitude-normalized, and partially enlarged images are shown in Figure 12. Due to the existence of the squint angle, each segment of the image generated by the RDS algorithm has geometric distortion, which is especially obvious at the splicing of each segment. Moreover, since the positions of adjacent scatters in the template are shifted after the imaging process, the image is blurred, and the ghost targets generated by the Doppler center frequency shifting in the azimuth dimension will be more obvious after the amplitude normalization. Actually, for the same reason, the brightness of the image is weakened as well, this phenomenon can be seen in Figures 13 and 14. These problems are solved by the TDFS-TS algorithm which corrected the geometric distortion caused by the squint angle.



(a)



(b)

Figure 11. Imaging results of the fake scene in Figure 10 using (a) the RDS algorithm and (b) the TDFS-TS algorithm. Parts of the images marked by rectangular boxes are enlarged and shown in Figure 12.

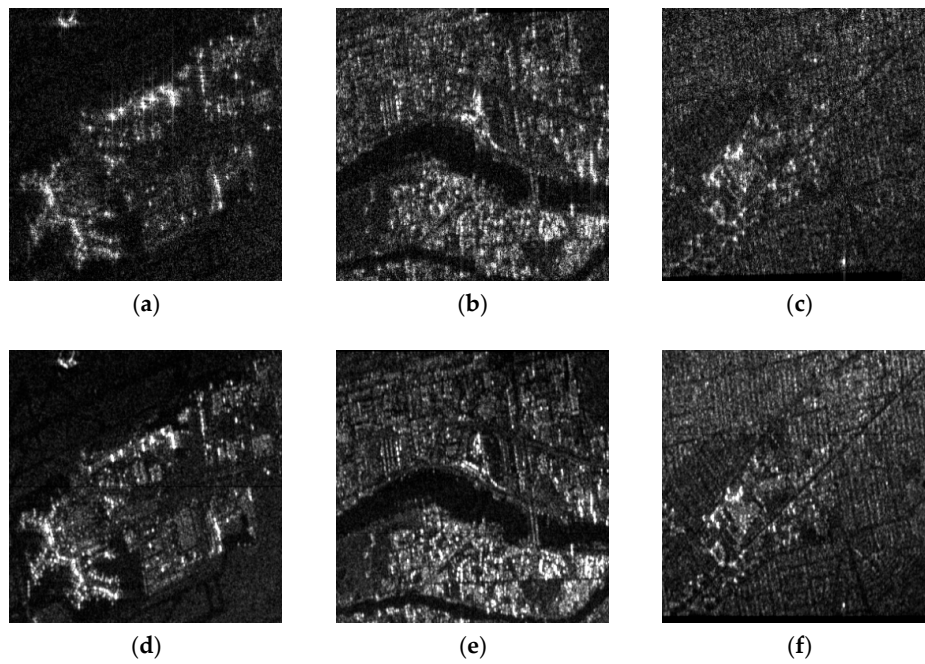


Figure 12. Partially enlarged image of Figure 11. (a–c) are the partial enlargement of the image generated by the RDS algorithm in the yellow, green, and red boxes, respectively; (d–f) are the partial enlargement of the image generated by the TDFS-TS algorithm in the yellow, green, and red boxes.



(a)



(b)

Figure 13. *Cont.*

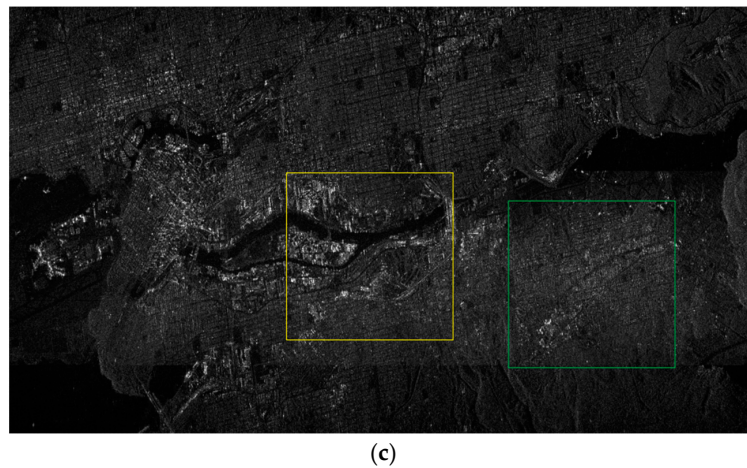


Figure 13. Comparison of jamming results. (a) is the image formed by the original signal, (b) is the image formed by the superposition of the original signal and jamming signal generated by the RDS algorithm, and (c) is the image formed by the superposition of the original signal and jamming signal generated by the TDFS-TS algorithm. Parts of the images marked by rectangular boxes are enlarged and shown in Figure 14.

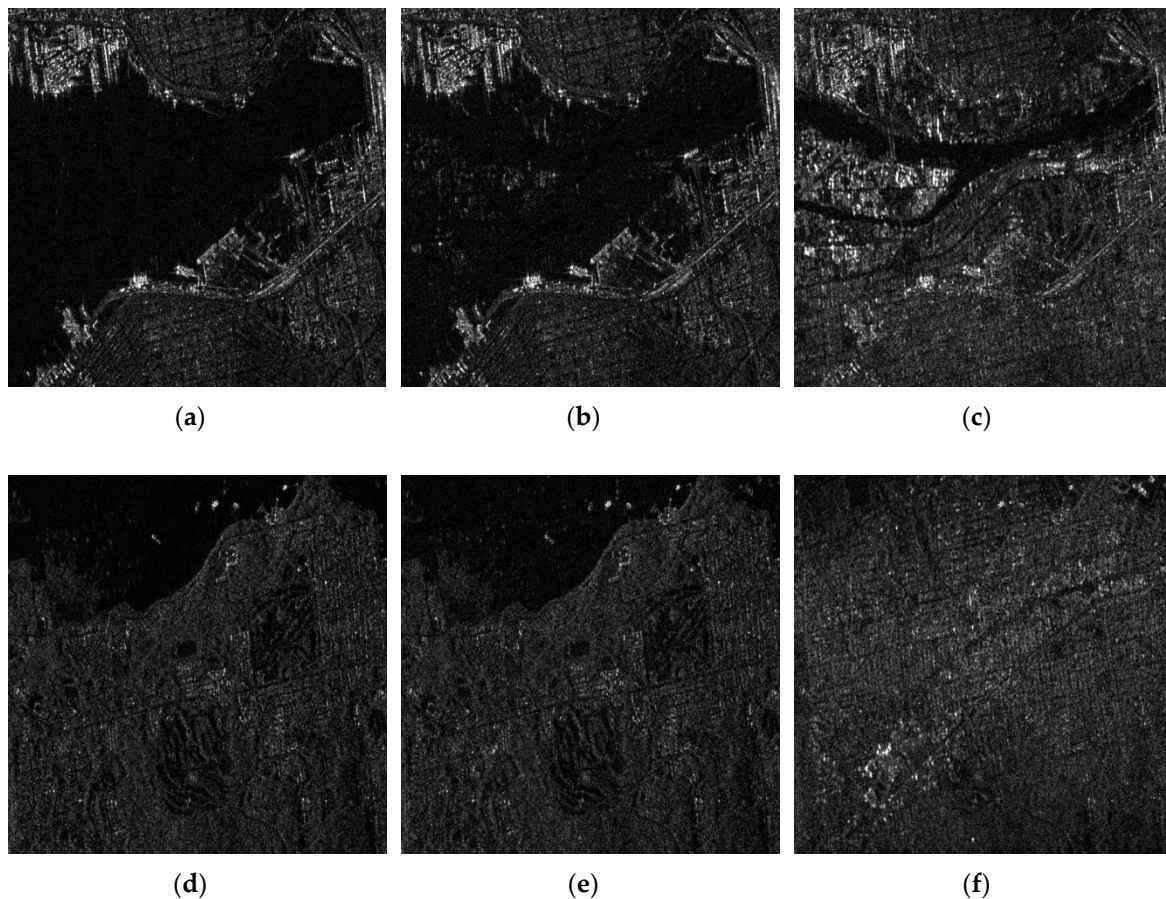


Figure 14. Partially enlarged image of Figure 13. (a–c) are the partial enlargement of the original image, the jamming image of the RDS algorithm, and the TDFS-TS algorithm, respectively in the yellow rectangular boxes; (d–f) are the partial enlargement of the original image, the jamming image of the RDS algorithm, and the TDFS-TS algorithm, respectively in the green boxes.

The imaging results of the superposition of the jamming signal and original signal are shown in Figure 13, and partially enlarged images are shown in Figure 14. It can be seen that the TDFS-TS

algorithm achieves a good deception effect, generating clear false targets such as land and buildings and changing the topographic structure of the protected area. However, the fake scene generated by the RDS algorithm is not obvious, mainly because of the decrease in brightness caused by geometric distortion. The jamming power has to increase in order to achieve a satisfactory jamming purpose, but the ghost targets will be strengthened at the same time. In conclusion, the TDFS-TS algorithm has certain advantages compared with the RDS algorithm in large-scene jamming.

3.3. Computational Complexity Analysis

The effectiveness of the TDFS-TS algorithm is verified by simulation in the previous subsection. In this subsection, we will estimate the computational complexity of the TDFS-TS algorithm to assess its practical value. Assume that the jamming scene template consists of $m \times n$ point scatters and is divided into $M \times N$ blocks, each block contains $U \times V$ point scatters. Here, for ease of analysis, the addition, multiplication and power operations are all considered to be a basic operation. The following will analyze the number of basic operations to obtain the JSF $H(f_r, t_a)$ at a specific frequency f_r and azimuth time t_a .

In the preprocessing stage, calculating an element of matrix \mathbf{Hr}_1 requires 15 basic operations, and the operation amount of all elements is $15V$; however, because the elements in \mathbf{Hr}_1 are actually a geometric series, the other elements can be generated by multiplying the first element by the common ratio, meaning that the amount of calculation is reduced to $15 + V$. According to the same analysis, the operation amount of \mathbf{Hr}_2 is $12 + U$, so the total computational complexity in the preprocessing stage is

$$C_{pre} = 15 + V + 12 + U = U + V + 27. \quad (43)$$

In the real-time calculation stage, calculating the JSF of a block center requires 20 basic operations, and a total of $20MN$ operations are required for all blocks. The operation amount for calculating matrix \mathbf{Ha}_{q1} is $15 + V$, which needs to be repeated N times. The calculation amount of matrix \mathbf{Ha}_{q2} is $14 + U$ and needs to be repeated N times as well. The computational complexity of matrix multiplication in Equation (42) is $2UV + U + 2V - 1$, so the operation amount of Equation (42) is $2UV + U + 2V$ added to the multiplication with $H_{c_{pq}}(f_r, t_a)$, and the calculation of Equation (42) needs to be repeated MN times. Finally, the operation amount of the summation—i.e., Equation (32)—is $MN - 1$. Based on the analysis above, the total amount of computation in the real-time calculation stage is

$$\begin{aligned} C_{rt} &= 20MN + N(15 + V) + N(14 + U) + MN(2UV + U + 2V) + MN - 1 \\ &= mn\left(2 + \frac{2}{U} + \frac{1}{V} + \frac{21}{UV}\right) + n\left(1 + \frac{U}{V} + \frac{29}{V}\right) - 1. \end{aligned} \quad (44)$$

According to the same analysis method, the computational complexity of different jamming algorithms including TDFS-TS, RDS, TDFS-TS without squint correction (TDFS-TS-WSC) and the basic algorithm (BA) shown by Equation (3) is derived and shown in Table 4.

Table 4. Computational complexity comparison of different algorithms.

	TDFS-TS	RDS ¹	TDFS-TS-WSC	BA
Preprocessing	$U + V + 27$	$mn\left(14 - \frac{1}{V}\right)$	$2UV - U + V + 11$	-
Real-time calculation	$mn\left(2 + \frac{2}{U} + \frac{1}{V} + \frac{21}{UV}\right) + n\left(1 + \frac{U}{V} + \frac{29}{V}\right) - 1$	$\frac{22mn}{V} - 1$	$\frac{21mn}{UV} + \frac{n}{V}(3U + 13) - 13$	$21mn - 1$

¹ the segment length in the range dimension of the RDS algorithm is the same as the block size of the TDFS-TS algorithm.

The block size U and V are determined by the parameters of the jamming object, the scatter density of the template, and the two imaging quality control factors ε and η . We fix U and V and observe the relationship between the computational complexity and the template size m and n . According to the simulation parameters in Section 4.1, we set $U = 267$ and $V = 539$, draw the relationship between

the computational complexity and the total number of scatters in the template shown in Figure 15. Here, for the convenience of analysis, we set $m = n$ and take the logarithm of computational amount for display.

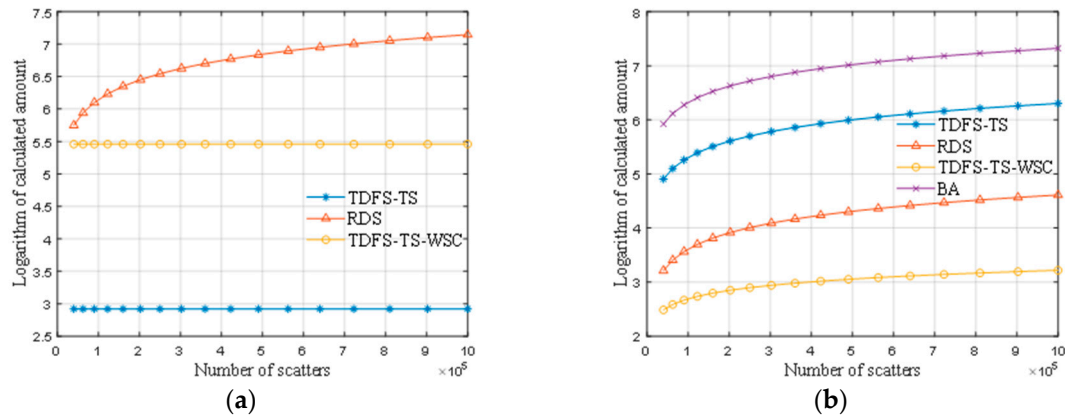


Figure 15. The relationship between the computational complexity and the total number of scatters in the template. (a) is the computational complexity in the preprocessing stage and (b) is the computational complexity in the real-time calculation stage.

It can be seen that, no matter in the preprocessing stage or in the real-time calculation stage, the computational complexity of the TDFS-TS-WSC algorithm is less than that of the RDS algorithm. In particular, in the real-time calculation stage, the computational complexity can be reduced by more than one order of magnitude because the TDFS algorithm in Equation (31) simplifies the calculation procedure significantly. When the squint correction is added, the calculation amount in the preprocessing stage is reduced, but increased in the real-time calculation stage.

4. Discussion

4.1. Imaging Quality

According to the analysis of the TDFS-TS algorithm in Sections 2.2.2 and 2.2.4, the simplification in the range dimension leads to a distortion of the azimuth profile including the main lobe broadening and position offset (in the squint mode), and the residual RCM introduced by the simplification in the azimuth dimension affects both the range and the azimuth profile. In addition, the inherent limitations of jamming signal, namely the Doppler bandwidth loss of the fake scatter far away from the jammer in the azimuth dimension, will broaden the azimuth main lobe. In summary, we can draw the following conclusions on the TDFS-TS algorithm:

1. The imaging quality of the jamming signal in the range dimension depends on the azimuth position of the false scatter ;
2. The distortion of the azimuth profile depends on both the range and the azimuth position of the false scatter;
3. These distortions become severe as the distance between the fake scatter and the block center increases.

These phenomena can be seen clearly in Table 2: P_0 and P_1 are both at the azimuth center of the block, thus they have the same imaging quality parameters in the range dimension; the imaging quality parameters of P_2 and P_3 in the range dimension are the same, and worse than that of P_0 and P_1 because the two points are both in the azimuth edge of the block; the situation in the azimuth dimension is more complicated: affected by both the range and azimuth position, the four points have different degrees of azimuth distortion, where P_3 is the worse and P_0 is the best; the impact of residual RCM

in the azimuth dimension is greater than that of azimuth chirp rate error by comparing the imaging quality parameters of P_1 and P_2 .

From Table 2 it can be seen that, in the broadside mode, the main lobe positions of P_2 and P_3 in the range dimension are slightly shifted. This is caused by the residual RCM as well. Due to the existence of residual RCM, the curve of jamming signal after RCM correction in the range-Doppler domain is not a straight line but a parabola which is expressed as Equation (22), thus the main lobe in the range dimension will shift towards the negative direction besides broadening. In the squint mode, the effect of residual RCM is more complicated, which can be seen in Table 3. Due to the nonlinear nature of the RCM error shown in Equation (22), the offset in the range dimension expressed in Equation (34) is just an approximation. In fact, it can hardly be eliminated completely, thus the images of P_1 , P_2 , and P_3 shift to varying degrees in the range dimension. In addition, by comparing the range offset of P_1 and P_2 , we can consider that the range coordinate has a greater effect on the range offset in the squint mode. Although the TDFS-TS algorithm cannot correct the range offset accurately, the maximum residual offset shown in Table 3 is approximately equal to the range resolution, and has little impact on the deceptive image shown in Figures 11–13.

In the squint mode, the offset in the azimuth dimension caused by the frequency modulation rate error can be effectively corrected by the TDFS-TS algorithm; the results are shown in Table 3. As a comparison, the RDS algorithm divides the template in the range dimension as well, thus the problem of frequency modulation rate error still exists. Without a correction algorithm, the main lobe position of the RDS algorithm shift severely in the azimuth dimension and the image is distorted. In short, the imaging quality of the TDFS-TS algorithm can be guaranteed both in the broadside mode and in the squint mode with a small squint angle.

4.2. Computational Efficiency

According to the results in Section 3.3, in the broadside mode, the TDFS-TS-WSC algorithm has a quite high computational efficiency, and the squint correction is time-consuming. This is because the range coordinate correction is related to the azimuth coordinate and the azimuth coordinate correction is also related to the range coordinate. Therefore, the range and azimuth coupling terms are added, resulting in a large number of calculations needing to be completed in the real-time calculation stage, and the computational efficiency becomes worse. However, due to the calculation of each block being completely independent in the TDFS-TS algorithm and the introduction of matrix operations, it is convenient to apply parallel computing technology to greatly increase the calculation speed. Therefore real-time jamming is feasible. In summary, compared with the RDS algorithm, the TDFS-TS algorithm is more efficient in the broadside mode, and the application scenario can be extended to the squint mode.

5. Conclusions

In this paper, the large-scene electromagnetic deception of SAR is studied. The primary focus is to reduce the computational burden during the jamming process. For this purpose, the TDFS algorithm is proposed, which can improve the computational efficiency significantly. In addition, the focus capability of the jamming signal must be considered. In order to ensure the deceptive image quality of the TDFS algorithm in a large scene, the template is divided into several blocks according to the SAR parameters and imaging quality control factor. The correction algorithm in squint mode is introduced so that the TDFS-TS algorithm can be used to the SAR with a low squint angle and medium aperture length. Finally, simulation results and computational complexity analyses show that, compared to other jamming algorithms, the TDFS-TS algorithm has higher computational efficiency with less image quality decline in the broadside mode. Furthermore, the application of parallel computation can partially compensate for the computational performance decline in the squint mode.

The TDFS-TS algorithm is applicable to space-borne SAR operating at broadside mode or a low squint angle mode. In the future, we will investigate the rapid jamming method against the SAR

with a significant squint angle and long synthetic aperture. Additionally, other problems such as intelligence gathering and gain control will also be studied.

Author Contributions: Conceptualization and supervision, W.Y.; formal analysis, F.M.; methodology, K.Y. and F.M.; experiment, G.L. and Q.T.; writing, K.Y. All authors have read and agreed to the published version of the manuscript.

Funding: This research was funded by Science and Technology on Complex Electronic System Simulation Laboratory, grant number DXZF-JC-ZZ-2017-007.

Conflicts of Interest: The authors declare no conflict of interest.

References

1. Walter, W.G. *Synthetic Aperture Radar and Electronic Warfare*; Artech House: Boston, MA, USA, 1993; pp. 25–39.
2. Condley, C.J. Some system considerations for electronic countermeasures to synthetic aperture radar. In Proceedings of the IEE Colloquium on Electronic Warfare Systems, London, UK, 14 January 1991.
3. Dumper, K.; Cooper, P.S.; Wons, A.F.; Condley, C.J.; Tully, P. Spaceborne synthetic aperture radar and noise jamming. In Proceedings of the 1997 Radar Edinburgh International Conference, Edinburgh, UK, 14–16 October 1997; pp. 411–414.
4. Fouts, D.J.; Pace, P.E.; Karow, C.; Ekestorm, S.R.T. A single-chirp false target radar image generator for countering wideband imaging radars. *IEEE J. Solid State Circuits* **2002**, *37*, 751–759. [[CrossRef](#)]
5. Kristoffersen, S.; Thingsrud, O. The EKKO II synthetic target generator for imaging radar. In Proceedings of the 5th European Conference on Synthetic Aperture Radar, Ulm, Germany, 25–27 May 2004; pp. 871–874.
6. Wei, Y.; Hang, R.; Shuxian, Z.; Li, Y. Study of noise jamming based on convolution modulation to SAR. In Proceedings of the 2010 International Conference on Computer, Mechatronics, Control and Electronic Engineering, Changchun, China, 24–26 August 2010; pp. 169–172.
7. Garmatyuk, D.S.; Narayanan, R.M. ECCM capabilities of an ultrawideband bandlimited random noise imaging radar. *IEEE Trans. Aerosp. Electron. Syst.* **2002**, *28*, 1243–1255. [[CrossRef](#)]
8. Yan, Z.; Guoqing, Z.; Yu, Z. Research on SAR jamming technique based on man-made map. In Proceedings of the International Conference on Radar, Shanghai, China, 16–19 October 2006; pp. 1–4.
9. Lin, X.; Liu, P.; Xue, G. Fast generation of SAR deceptive jamming signal based on inverse range doppler algorithm. In Proceedings of the IET International Radar Conference, Xi'an, China, 14–16 April 2013; pp. 1–4.
10. Xiaodong, H.; Jun, Z.; Jun, W.; Dongping, D.; Bin, T. False target deception jamming for countering missile-borne SAR. In Proceedings of the IEEE 17th International Conference on Computational and Engineering, Chengdu, China, 19–21 December 2014; pp. 1974–1978.
11. Feng, Z.; Bo, Z.; Mingliang, T.; Xueru, B.; Bo, C.; Guangcai, S. A Large scene deceptive jamming method for space-borne SAR. *IEEE Trans. Geosci. Remote Sens.* **2013**, *51*, 4486–4495. [[CrossRef](#)]
12. Qingyang, S.; Ting, S.; Shicheng, Z.; Bin, T.; Wenxian, Y. A novel jamming signal generation method for deceptive SAR jammer. In Proceedings of the IEEE Radar Conference, Cincinnati, OH, USA, 19–23 May 2014; pp. 1174–1178.
13. Bo, Z.; Feng, Z.; Zheng, B. Deception jamming for squint SAR based on multiple receivers. *IEEE J. Sel. Top. Appl. Earth Obs. Remote Sens.* **2015**, *8*, 3988–3998. [[CrossRef](#)]
14. Bo, Z.; Lei, H.; Feng, Z.; Jihong, Z. Performance improvement of deception jamming against SAR based on minimum condition number. *IEEE J. Sel. Top. Appl. Earth Obs. Remote Sens.* **2017**, *10*, 1039–1055. [[CrossRef](#)]
15. Qingyang, S.; Ting, S.; Kaibor, Y.; Wenxian, Y. Efficient deceptive jamming method of static and moving targets against SAR. *IEEE Sens. J.* **2018**, *18*, 3601–3618. [[CrossRef](#)]
16. Yongcai, L.; Wei, W.; Xiaoyi, P.; Dahai, D.; Dejun, F. A Frequency-domain three-stage algorithm for active deception jamming against synthetic aperture radar. *IET Radar Sonar Navig.* **2014**, *8*, 639–646. [[CrossRef](#)]
17. Yongcai, L.; Wei, W.; Xiaoyi, P.; Qixiang, F.; Guoyu, W. Inverse omega-K algorithm for the electromagnetic deception of synthetic aperture radar. *IEEE J. Sel. Top. Appl. Earth Obs. Remote Sens.* **2016**, *9*, 3037–3049. [[CrossRef](#)]
18. Bo, Z.; Lei, H.; Jian, L.; Maliang, L.; Jinwei, W. Deceptive SAR jamming based on 1-bit sampling and time-varying thresholds. *IEEE J. Sel. Top. Appl. Earth Obs. Remote Sens.* **2018**, *11*, 939–950. [[CrossRef](#)]

19. Yongcai, L.; Wei, W.; Xiaoyi, P.; Letao, X.; Guoyu, W. Influence of estimate error of radar kinematic parameter on deception jamming against SAR. *IEEE Sens. J.* **2016**, *16*, 5904–5911. [[CrossRef](#)]
20. Franceschetti, G.; Guida, R.; Iodice, A.; Riccio, D.; Ruello, G. Efficient simulation of hybrid stripmap/spotlight SAR raw signals from extended scenes. *IEEE Trans. Geosci. Remote Sens.* **2004**, *42*, 2385–2396. [[CrossRef](#)]
21. Ahmed, S.K.; Laurent, F.F.; Eric, P. Efficient SAR raw data generation for anisotropic urban scenes based on inverse processing. *IEEE Geosci. Remote Sens. Lett.* **2009**, *6*, 757–761. [[CrossRef](#)]
22. Ian, G.C.; Frank, H.W. *Digital Processing of Synthetic Aperture Radar Data: Algorithms and Implementation*; Artech House: Boston, MA, USA, 2005; pp. 45–63.
23. Yongcai, L.; Wei, W.; Xiaoyi, P.; Dahai, D. Effective region of active decoy jamming to SAR based on time-delay doppler-shift method. *J. Radars* **2013**, *2*, 46–53.



© 2019 by the authors. Licensee MDPI, Basel, Switzerland. This article is an open access article distributed under the terms and conditions of the Creative Commons Attribution (CC BY) license (<http://creativecommons.org/licenses/by/4.0/>).